

Two-axis scanning LIDAR using a liquid crystal control

Seiji Nishiwaki (✉ wside@nifty.com)

Technology Division, Panasonic Corporation

Research Article

Keywords: LiDAR, liquid crystal, grating coupler, TOF, waveguide, laser beam, rod lens

Posted Date: March 22nd, 2021

DOI: <https://doi.org/10.21203/rs.3.rs-344134/v1>

License:  This work is licensed under a Creative Commons Attribution 4.0 International License.

[Read Full License](#)

Two-axis scanning LIDAR using a liquid crystal control

Seiji Nishiwaki

Technology Division, Panasonic Corporation,
3-1-1 Yagumo-nakamachi, Moriguchi City, Osaka 570 - 8501, Japan

Correspondence to: Seiji Nishiwaki (e-mail: wside@nifty.com)

Abstract

Sophisticated non-mechanical technology for LIDARs is needed to realize safe autonomous cars. We have confirmed the operating principle of a non-mechanical LIDAR by combining concentric circular-grating couplers (CGCs) with a coaxially aligned rod lens. Laser light incident vertically on the center of the inner CGC along the center axis of the lens is radiated from the outer CGC and passes through the side surface of the lens. It is converted to a parallel beam that scans in two axes by applying voltages to two area-segmented electrode layers sandwiching the CGCs and a liquid crystal layer formed on the CGCs. We have demonstrated scanning whose motion ranges were 360 degrees horizontally and 10 degrees vertically. A beam with a spread angle of 0.3×0.8 degrees at a minimum swept vertically up to a frequency of 100 Hz and ten equally spaced beams scanned rotationally with a 6-degree cycle variation of spread of between 0.8 and 3.5 degrees.

Introduction

Aiming for completion in the next few years, auto manufacturers and information equipment manufacturers across the globe are advancing the development of fully autonomous cars. To realize this “level 3,” real-time measurement technology of distance between cars and physical objects is necessary. LIDAR (Light detection and ranging) apparatus using time of flight (TOF) technology is one potential solution. Conventional LIDARs are composed of a mechanical structure¹⁻³ such as a polygon mirror or a galvanic mirror mounted on a rotating plate. The downside of this type is that they are expensive, slow, large, heavy, and non-durable due to having moving parts. To overcome these drawbacks, various non-mechanical methods (e.g., solid state LIDAR or SS-LIDAR) have been proposed.

A MEMS (microelectromechanical system) mirror⁴⁻⁷ or an optical phased array⁸⁻¹⁶ (OPA) can be used for SS-LIDAR. A MEMS mirror is fabricated by etching a silicon crystal and forming a coil structure. The direction of a light ray incident on the mirror surface can be controlled by the Lorentz force produced by energization of the coil. MEMS-LIDAR is likely the most advanced non-mechanical type, but it faces problems with durability because it still has moving parts. Moreover, it is difficult to steer it free from hysteresis caused by creep and it is also easily affected by automotive vibrations due to the use of a resonant mode (non-linear mode) for scanning in the horizontal direction. For the OPA, although phased arrays are practically realized in the field of radio wave technology, manufacturing challenges remain with the fine-pitched fabrication process that is required. It is also difficult to control the phases emitted from each array and to correct for environmental changes during use.

Another proposition provides a good light sweeper by using a slow-light waveguide¹⁷⁻¹⁹, in which light is transported with the slow group velocity in multiple layers or photonics crystals. However, few slow-light methods appear to be suitable for commercial use because their beam steering that exploits wavelength changes requires an expensive light source.

Some electro-optic structures^{20,21} and photonic-crystal lasers²² give provide a good light scanner, but they are limited to one-dimensional steering.

All the above-mentioned SS-LIDARs significantly narrow their steering ranges to realize non-mechanical scanning and most of them (except for MEMS-LIDARs) need detection structures that are physically separate from their emission structures. To provide a robust answer to these challenges, we devised a novel structure (named CGC-LIDAR) and demonstrated the light-scanning principle.

Structure and operational principle of a CGC-LIDAR

Figures 1a and 1b are a perspective and cross-sectional illustration of a CGC-LIDAR that includes concentric grating couplers (CGCs)²³⁻²⁵. Light of wavelength $\lambda = 0.94 \mu\text{m}$ emitted from a laser diode is collimated to parallel light by a collimator and is reflected to a polarizing beam splitter (PBS). It is then focused by a focal lens on the inner CGC, passing through a 1/4 wave plate, a half mirror, and the rod lens along axis L. The circularly polarized light vertically incident on the CGC excites the guided light in TE mode in the waveguide layer, contacting which propagates uniformly from the center to outside. The guided light is radiated from the coupler C and is concentrated near point F_1 by LC (liquid crystal) control. It is then converted to a parallel beam by refraction at the side surfaces of the rod lens. Five parallel beams are generated equiangularly around the rod lens and are rotated by LC control. Diffused light reflected from an outer object returns to the coupler C in the opposite direction. The return light output from the coupler A is detected by photodiodes A and B. TOF signals are produced by the two detectors. Our method produces multi-sweep beams in principle, and these beams also produce individual TOF signals. They can be separated by using the two detectors (see Supplementary Information S1).

CGC-LIDAR is built up concentrically with an RLE (rod lens element) and a CGCP (CGC plate) which are joined with a matching oil of refractive index 1.59. The RLE consists of a rod lens (radius $r_0 = 0.95 \text{ mm}$) and a CP (circularly perforated) plate, which are built along axis L and fastened together with a joint that aligns their bottom surfaces (see Supplementary S2). The CGCP is built of a quartz plate and an HR (high refractive index, index 2.0) plate by encapsulating a $5 \mu\text{m}$ -thick LC layer, made of 5CB.

On the LC-side surface of the quartz plate, an aluminum (Al) layer ($0.09 \mu\text{m}$ thick), a SiO_2 (silicon oxide) layer ($t_0 = 1.16 \mu\text{m}$ thick) and a Ta_2O_5 (tantalum oxide) layer ($t_1 = 0.132 \mu\text{m}$ thick) are formed sequentially. The Al layer acts as an electrode and is divided from inside to outside into three areas: A, B, and C (radius 0 - 0.10 mm, 0.30 - 4.01 mm, and 4.50 - 7.00 mm).

As shown in Figs. 1c-1d, concentric circular gratings ($d = 0.013 \mu\text{m}$ deep) divided into three areas of A, B, and C (radius 0 - 0.05 mm, 0.05 - 4.50 mm, and 4.50 - 6.50 mm) are formed concentrically along the axis L by electron lithography on the SiO_2 layer after a planarizing process using CMP (chemical mechanical polishing). The SiO_2 layer acts as a buffer layer and the Ta_2O_5 layer acts as a waveguide. While the gratings in areas A and C behave as grating couplers because their grating pitches ($\Lambda_A = 0.544$ and $\Lambda_C = 0.295 \mu\text{m}$) are larger than the critical level of coupling ($0.27 \mu\text{m}$), the grating area B does not behave as a coupler because its pitch ($\Lambda_B = 0.240 \mu\text{m}$) is smaller. The duty rate of the gratings in area A and B are 0.5, and that in C is 0.2 (see Supplementary S3).

Whereas, a SiN (silicon nitride) layer ($0.10 \mu\text{m}$ thick) and an ITO (indium tin oxide) layer ($0.10 \mu\text{m}$ thick) are formed on the LC-side surface of the HR plate. Concentric

circular gratings (0.05 μm deep, period $\Lambda_D = 1.2 \mu\text{m}$) are concentrically formed from inside to outside by reduced projection exposure along the axis L on the surface of the SiN layer. The ITO layer behaves as an electrode, and in the same way as the Al layer, is divided into three areas: A, B, and C.

As shown in Fig. 1e, the electrode B is further divided into 60 areas of B_k ($k = 0$ to 59) in the rotational direction. The electrode C is divided into halves to lace wires to the outside. While electrodes A and C have the same shapes between the Al layer and the ITO layer, the B_k electrodes, which have a zigzag shape (see Supplementary S4), are reversed between them. Although the B_k electrodes do not need wiring because their shapes are equivalent to wiring, they must use the spaces between electrodes B and C (i.e., radius 4.01 - 4.50 mm) to link them to the outside. For electrode A, one electrode of B_k is used as a wire instead. Rectangular or triangular AC (alternating current) voltages of cycle t_A , t_B , and t_C , respectively, are applied to electrodes A, B, and C. While an envelope waveform of constant AC amplitude is applied to electrode A, varying waveforms are applied to the electrodes of B_k and C with cycle T_B and T_C , which are related to beam sweeping cycles in the horizontal and vertical directions. Since the AC signals are reversed between the Al electrode and the ITO electrode, the differences in voltages between them are doubled.

The LC layer sandwiched by the two plates is homogeneously aligned in the rotational direction around the axis L due to the orientation force of the gratings remaining on the surfaces of the Ta_2O_5 layer and the ITO layer. As shown in Fig. 1f, when AC signals are applied to the electrodes, the alignment of the LC molecules is raised in a plane contacting both the thickness direction of the LC and the grating direction. The effective refractive index (ERI) of N for the guided light declines as a function of increasing AC amplitude due to change of n_L (i.e., the refractive index of the LC layer for the guided light of TE mode).

The voltage control of electrode A optimizes the coupling conditions at the coupler A. The voltage of electrode C controls the vertical scan according to the formula of $n_L \sin \theta_L = \lambda / \Lambda_C - N$, where θ_L is the radiation angle in the LC layer (see Supplementary S2). The waveforms applied to the B_k electrodes adjust the focusing position and convert the radiated light to five parallel beams (see Supplementary S5). Rotation of this waveform produces a horizontal scan around the axis L.

Beam-collimating and rotating principle in the horizontal direction

Figures 2a shows a portion of an electrode pair composed of the ITO and Al electrode, in which vertexes of zigzag shapes between the two electrodes of B_k overlap together and diamond shape electrodes such as b_{2k} and b_{2k+1} are aligned in the radial direction, where b_{2k} are generated from the combination of Al electrodes B_k and ITO electrodes B_k , and b_{2k+1} are

from Al electrodes B_k and ITO electrodes B_{k+1} . The voltage amplitude at the electrodes b_{2k+1} becomes the average between those at the electrodes b_{2k} and the electrodes b_{2k+2} . When the AC signals are applied to the electrodes of B_k , the ERIs of such as N_{2k} or N_{2k+1} , in response to the voltages v_{2k} or v_{2k+1} at electrodes b_{2k} or b_{2k+1} , are aligned in the radial direction.

Figures 2b show examples of voltage waveforms applied to the B_k electrodes. For a non-rotating condition (or a static state), the AC waveform envelopes are constant, with their signal amplitudes varying sinusoidally according to the value of k . Amplitude distribution between the electrodes allows the beams to be collimated. Under rotating conditions, the envelopes have a sinusoidal shape and the phase between the neighbor signals shifts together by $1/60f_H$. Collimated beams can be rotated by applying a phase shift to the sinusoidal amplitude.

Figure 2c shows relationships under a static condition between a voltage waveform V_B applied to the B_k electrodes and the response of the ERI to an azimuth angle φ ($= 2k\pi/60$ or $(2k+1)\pi/60$). The waveform V_B has a periodic number m ($m = 5$ or 10) per revolution and is represented by a collection of elements of v_{2k} or v_{2k+1} . N_{2k} (or N_{2k+1}) is given from v_{2k} (or v_{2k+1}) and its curve traces a shape that is the inverse of waveform V_B . If $N_{2k+1} > N_{2k}$ as shown in Fig. 2c, the guided light (shown by the red arrow in Fig. 2a) deflects to the higher index side (in the direction of the blue circling arrows) at the intersection with the boundary of the diamond-shaped electrodes. The differences in indexes are small. However, since the guided light passes through more than 30 boundaries within the range of area B, the accumulated deflection angle of the red arrow eventually totals about 10 degrees in comparison with the blue and straight arrow. This deflecting principle is similar to that of an electro-optic scanner²⁰. The rotating condition corresponds to the movement of the waveform at a frequency f_H as indicated by an arrow shown in Fig. 2c (see supplementary S6).

Figure 2d shows a combination of a perspective illustration of light radiated from the coupler C and a cross-sectional drawing of light refracted at the rod lens surface. Figure 2e shows a ray-tracing result for light that propagates in the guided layer, is then radiated from the coupler C, and penetrates RLE. If no difference in voltage is applied to the B_k electrodes, the guided light propagates in the direction of the blue arrow in Fig. 2a: the radiated light is focused at point F_0 on the center axis L of the rod lens and travels in a straight line in the radial direction as shown by the blue lines in Figure 2d. In this case, the radiated light becomes a widely spread beam with a conical surface. When applied to the B_k electrodes, the guided light propagates in the direction of the red arrow in Fig. 2a and the radiated light is focused on point F_1 , which moves the distance of f_0 from F_0 . The light becomes a parallel beam after refraction at the side surface of the rod lens, as shown by the

red dotted lines. This beam is generated by the period number m of the waveform, that is, five or ten. To correct the aberration of the parallel beams, the light focused on F needs a phase difference of $n_0 f_0 (1 - \cos\varphi)$,

$$\text{where } f_0 = \frac{r_0 \sin \psi}{n_0 \sin \varphi}, \quad \sin \psi = \frac{n_0 \sin \varphi \sqrt{n_0^2 + 1 + 2n_0 \cos \varphi}}{\sqrt{(n_0^2 - 1)^2 + 4n_0^2 \sin^2 \varphi}}.$$

Therefore, the difference in ERI caused in the range of the area B (radius r_1 to r_2) becomes $\Delta N = \frac{n_0 f_0 (1 - \cos\varphi)}{r_2 - r_1}$, as shown in Figure 2f.

The focal line L_1 generated by the aggregate of point F_1 is not actually parallel with the axis L , and slightly lists so as to broaden towards the top. Therefore, to correct the aberrations caused in the wide range in the radial direction, an inverted truncated cone is better than a rod shape.

Analytical results for coupling characteristics and design condition

Coupling lengths are different between coupler A and C. Although input-coupling efficiency is important for coupler A, the radiation range is important for coupler C to ensure parallelism of the radiated light, because the angle of spread is inversely proportional to the radiation range. When the depth of gratings is equal in couplers A and C, it is difficult to balance their coupling conditions. We can find the design condition by using Figures 3a-3f, where the incident light is subject to linear polarization.

Figures 3a - 3c show the responses of input-coupling efficiency at coupler A to the buffer layer thickness t_0 , coupling length L , and wavelength λ , respectively, with the parameters of the refractive index n_L of the LC layer. Figure 3a is calculated by 3D-FDTD for $\lambda = 0.94 \mu\text{m}$, $\Lambda = 0.54$ and $0.55 \mu\text{m}$, $t_1 = 0.14 \mu\text{m}$, groove depth $d = 0.1 \mu\text{m}$, groove duty rate $\varepsilon = 0.5$, and diameter $L = 10 \mu\text{m}$.

Figures 3b and 3c result from 2D-FDTD for $\lambda = 0.94 \mu\text{m}$, $\Lambda = 0.55 \mu\text{m}$, $t_1 = 0.14 \mu\text{m}$, $t_0 = 1.16 \mu\text{m}$, $d = 0.02 \mu\text{m}$, and $\varepsilon = 0.5$ and for $\Lambda = 0.54$ and $0.55 \mu\text{m}$, $d = 0.02 \mu\text{m}$, $\varepsilon = 0.5$, $t_1 = 0.14 \mu\text{m}$, $t_0 = 1.16 \mu\text{m}$, and coupling length $L = 90 \mu\text{m}$, respectively. From Fig. 3a, a coupling efficiency exceeding 40 % is anticipated by controlling the thickness, and $t_0 = 1.16 \mu\text{m}$ appears to be appropriate for counteracting film thickness error. If the coupling length or grating depth of coupler C is sufficient, all the input-coupled light at coupler A is radiated from C and is converted to collimated beams.

From Figs. 3b and 3c, $L = 90 \mu\text{m}$ and $\Lambda = 0.544 \mu\text{m}$ are appropriate for maximizing the coupling efficiency. At the same time, by controlling the LC index n_L , sufficient efficiency for coupler A can be achieved by the design condition of $d = 0.02 \mu\text{m}$ and $\varepsilon = 0.5$.

Figures 3d - 3f show responses of a radiation decay factor α to groove depth d (where $\varepsilon =$

0.5 and $n_L = 1.60$), groove duty rate ε (where $d = 0.02 \mu\text{m}$ and $n_L = 1.60$), and LC index n_L (where $d = 0.02 \mu\text{m}$ and $\varepsilon = 0.25$) with parameters of a wavelength λ , calculated by 2D-FDTD for $\Lambda = 0.30 \mu\text{m}$, $t_1 = 0.14 \mu\text{m}$, and $t_0 = 1.16 \mu\text{m}$. From Figs. 3d - 3f, the factor α can be less than 2 mm^{-1} (that is, the radiation range can exceed 0.5 mm) under the design conditions of $d = 0.02 \mu\text{m}$ and $\varepsilon = 0.2$.

Based on the above results, coupler A is designed under the conditions of $\Lambda = 0.544 \mu\text{m}$, $d = 0.013 \mu\text{m}$, $\varepsilon = 0.5$ and radius $50 \mu\text{m}$, and coupler C is designed under the conditions of $\Lambda = 0.295 \mu\text{m}$, $\varepsilon = 0.2$ and $L = 1.5 \text{ mm}$.

Experimental system

We can observe a scanning beam radiated from the CGCP sample using the experimental system. Figure 4a shows a configuration diagram of the system (see Methods in detail). Figures 4b, 4c, and 4d show perspective photographs of a portion of the system, the RLE, and the CGCP. Figures 4e and 4f, respectively, are micrographs of the surface of the CGCP where the RLE is removed and located.

Light emitted from a DFB-LD (distributed-feedback laser diode) is collimated and vertically focused to the CGCP with circular polarization. Since a portion of the light incident to the CGCP is reflected from coupler A and the half mirror, the focused spot is observed with the RLE and the CGCP by a microscope camera. Light radiated from coupler C is converted from rotation at a constant angular velocity to a linear uniform motion using an f - θ lens. It is collimated by a relay lens and observed by an imaging camera. Control signals applied to the electrodes of the CGCP are produced in computer-controlled waveform generators and are magnified by an amplifier. Figure 4e is a photograph of a central surface of the CGCP under LC control, with the RLE removed. Since the refractive indexes of the LC layer change under LC control, the external appearance is rotated according to the rotation of the diamond shapes in the radial direction (see Supplementary Movie M1). Figure 4f shows an observation photograph of a light spot incident to the surface of the CGCP using a microscope. When the spot is adjusted at the center of coupler A, the radiation from coupler C is confirmed by the imaging camera attached to the f - θ lens.

Experimental Results

The voltage V_A for electrode A was set here to zero, because the amount of light radiated from coupler C reached its maximum for $V_A = 0$. This departure from the adjustable range may be due to a thickness error of t_1 (i.e., $0.140 \mu\text{m}$ designed vs. $0.132 \mu\text{m}$ measured).

Figure 5a shows the relationship between the amount of light radiated from the coupler C and the constant voltage V_B applied to the electrodes B_k with the cycle t_B of triangular AC

voltage as the parameter. When the cycle t_B was made longer than 2 ms, the spread angle increased gradually, expanding infinitely at over 10 ms. Whereas, when the cycle t_B was reduced to the range of 1/4 - 2.0 ms, the amount of guided light passing through the region of electrode B and radiated from coupler C declined and disappeared up to 0.1 ms. The reason appears to be that certain disclinations are generated in the region of electrode B, which disturb the rectilinear propagation of guided light. Thus, the cycle conditions were set here as $t_B = 1$ ms, and the periodic number is confined to $m = 10$, instead of $m = 5$, because deflective power increases with decreasing the curvature radius of a corrected wavefront by half.

As shown in Figure 5a, our sample was significantly affected by the frequency of AC voltage, but conventional LC devices including displays are believed not to be substantially affected. This is probably because while conventional devices exploit the change in alignment of the LC molecules across the layer thickness, our device exploits the change in the evanescent field of the guided light.

Figure 5b is an observation photograph indicating oriented states of the LC at the fringe region of the electrodes B and C, where electrode B is subject to a static state of $m = 10$ and $V_B = 3.2 - 40.0$ volts (distributed symmetrically about the x-axis) with $t_B = 1.0$ ms. As seen in Fig. 5b, some disclinations are seen at the higher voltage regions, resembling soap bubbles, along the etched lines of the ITO layer (see Supplementary S7).

Figures 5c and 5d show the vertical-steering performance for the voltage V_C applied to the electrode C with the cycle t_C of rectangular AC voltage as a parameter. They are measured under the same conditions for the electrode B shown in Figure 5b. In Fig. 5c, the vertical displacement (or the sensitivity of vertical motion) peaks in the range of $t_C = 1/8 - 1/32$ ms and becomes about 10 degrees for the applied voltage of 20 volts. (The displacement for $t_C = 1$ ms is half of that for $t_C = 1/8 - 1/32$ ms. Similarly, the maximum value of the refractive effect produced by the B_k electrodes for $t_B = 1$ ms will be also reduced by half. This is the reason that $m = 10$ was selected in this experiment.) As shown in Fig. 5d, the horizontal spread angles (FWHM of spread angle) are stable within 0.3 degrees in the range equal to or less than 1/16 ms, and the vertical ones are stable within 0.6 - 0.8 degrees for any cycle range.

Figures 5e1 – 5e3 show observation photographs of vertically sweeping beams radiated from the coupler C (corresponding to the area just visible in Fig. 5b) using the imaging camera of the f- θ lens (see supplementary movie M2). Their spots are generated by vibrating control of $t_C = 1/32$ ms and $V_C = 0 - 20.0$ volts for electrode C. The amount of light rises and falls between half of a sweep cycle: this can be explained by using the result of Fig. 3f, where the states of Figs. 5e1, 5e2, and 5e3 correspond to $n_L \geq 1.65$, ≈ 1.62 , and ≤ 1.59 for the curve of $\lambda = 0.94$ μm , respectively. In Figs. 5e1 and 5e3, the guided light

passes through the region of coupler C before being radiated. This problem will be easily solved by controlling the laser driver, because the change shows a regular cycle. The collimation condition is slightly changed with changes in the radiation angle, but it can be compensated by controlling the waveform shape of B_k according to the voltage of C.

Figure 5f shows the frequency response of the vertical displacement. We can see that the half maximum of the displacement amplitude is maintained up to 100 Hz.

Figures 5g show rotational sweeps in the rotational state of $T_B = 0.5$ sec for electrode B and the static state of $t_C = 1/16$ ms and $V_C = 15.0$ volts for electrode C (see supplementary S7 and movie M3).

Figure 5h shows image-analyzed results of a movie according to Figs. 5g. The amount of light is measured while stationary along the vertical line (according to argument $\varphi = 0$ degree of Fig. 5g or the x-axis direction of Fig. 5b) of 6 pixels' width from each image. The amount of light rises towards a peak over a cycle of 36 degrees. The variation of the peaks is due to the shortage of sampling numbers, which is a function of the frame rate of the image sensor. Figure 5i shows relationships between the spread angle and the rotating angle φ corresponding to the spots shown in Figure 5g. As shown in Fig. 5i, vertical spreads settle within 0.2 - 0.3 degrees and horizontal spreads vary over a 6-degree cycle (i.e., the divided angle of electrode B_k) at 0.8 - 3.5 degrees. This cycle change is caused by a deficit of phase correction for a single beam, because only three electrode lines per single beam can contribute to beam-collection as shown in Fig. 5b. The change could therefore be improved by, after overcoming problems such as disclinations, changing the periodic number from $m = 10$ to $m = 5$ or increasing the division number of electrode B.

Conclusion

We have demonstrated the world's first two-axis scanner using liquid crystal control in which the scanning ranges were 360 degrees in the horizontal direction and 10 degrees in the vertical direction: the beam of a spread angle of 0.3 x 0.8 degrees at minimum sweeps vertically up to 100 Hz frequency and ten equally-spaced beams scan rotationally with a 6-degree cycle variation of spread angle of between 0.8 - 3.5 degrees.

The performances of spread angles and motion ranges can be improved by dealing with challenges like the disclinations at high voltages. The sweep frequency can be also improved by changing the thickness of the LC layer from 5 μm to less than 0.5 μm , since our device exploits the change at the surface layer interface of the LC. Because the frequency response of the LC is inversely proportional to the square of the thickness, a sweep frequency of more than 10 kHz (or 50 kHz if we add the five-beams effect) can be anticipated.

Some mechanical LIDARs originally have a 360-degree scanning range in the horizontal

direction and their detection structures are used concomitantly with the emission structures. However, all conventional SS-LIDARs significantly narrow their ranges of motion to enable non-mechanical scanning, and most of them (except for MEMS-LIDARs) require detection structures that are separate from their emission structures.

Our CGC-LIDAR maintains a 360-degree scanning range and the detection and emission structures can be combined. Moreover, it produces multi-sweep beams that provide a higher-definition image enabling the “level 5,” and the S/N ratio of TOF signals detected using our method is anticipated to be 50-fold that achieved by conventional methods due to the effect of the wavelength selectivity of the coupler (see supplementary S8).

We believe our method closely matches the requirements of SS-LIDAR. We will aim in future to achieve better performance and will at the same time investigate the potential for a low-cost mass-fabrication process.

Materials and methods

Construction materials

The rod lens and CP plate are made of S-BSM14 by Ohara. The HR plate is made of BOC30 by Sumita. For the liquid crystal, 5CB (4-cyano-4'-pentylbiphenyl by TCI) is used.

Measuring equipment

Light emitted from a DFB-LD (EYP-DFB-0935 by Eagleyard) is collimated and shaped into a parallel beam with circular spread by a collimator (C230TMD-B mounted on LDH3-P1/M by Thorlabs) and a beam expander (anamorphic prism pairs #47-274 by Edmund). After a portion of light is split by a half mirror (Non-Polarizing Beam splitter CCM5-BS017/M by Thorlabs) and coupled by a fiber coupler (fiber port PAF2P-15B by Thorlabs), the light's wavelength is monitored by a light spectrum analyzer. The beam transmitted by the half mirror is adjusted by rotation of a $\lambda/2$ plate to minimize transmission through a polarization beam splitter (PBS, CCM5-PBS202 by Thorlabs). The light reflected from the PBS is circularly polarized by a $\lambda/4$ plate and is vertically focused to a CGCP by a focal lens ($f = 100$ mm). Since a portion of the incident light is reflected from coupler A and the half mirror (BS011 by Thorlabs), the focused spot is observed with the RLE and the CGCP using a microscope camera (DINOAM7915MZTL by Dino). The CGCP is located on a Peltier device (VPE20-30S by VICS) and is thermally controlled at 26 °C. The Peltier device is also located on the Gonio-stages and x- and y-stages for positioning. Light radiated from coupler C is converted by an f- θ lens (LSM05-BB by Thorlabs), collimated by a relay lens (LB1723-B by Thorlabs) and observed by an imaging camera that includes an image sensor (CM3-U3-13Y3M-CS by FLIR). The f- θ lens unit is set up on a vertically rotating mechanism. Voltage signals applied to the electrodes of the CGCP are produced in waveform generators (AWG-10 by Elmos) controlled by a computer and are magnified by

up to 4-fold by an amplifier.

Estimation of spread angles

Spread angle is estimated by calculating the standard deviation of an intensity distribution along the vertical or horizontal cross-section passing through a peak point driven from jpeg images. The intensity is an integer value from 0 – 255: some of the lower range can be cut off as noise. Since the cutoff level affects the calculated result of the spread angle, it must be carefully identified and selected. The level is set here at 3 % (the level for a black background) of 255.

Acknowledgements

The author thanks Y. Inoue for the initial incentive and T. Korenaga and T. Hirasawa for providing financial support for the development of devices.

Conflict of interest

We declare that we have no competing interests as defined by the Nature Publishing Group, or other interests that might be perceived to influence the results and/or discussion reported in this article.

Author contributions

S. N. devised the concept, designed and analyzed the experimental sample. He also established the experiment and evaluation system, carried out assessment experiments and monitored progress.

References

- [1] Wyant, J. C. Rotating Diffraction Grating Laser Beam Scanner, *Appl. Opt.*, **14**, 1057-1058 (1975).
- [2] Matsuda, T., Abe, F., and Takahashi, H. Laser printer scanning system with a parabolic mirror, *Appl. Opt.*, **17**, 878-884 (1978).
- [3] Varughese, K. O. G. and Krishna, K. S. R. Flattening the field of post-objective scanners by optimum choice and positioning of polygons, *Appl. Opt.*, **32**, 1104-1108 (1993).
- [4] Asada, N., Matsuki, H., Minami, K. and Esashi, M. Silicon Micromachined Two-Dimensional Galvano Optical Scanner, *IEEE Trans. Mag.*, **30**, 4647-4649 (1994).
- [5] Miyajima, H., Asaoka, N., Isokawa, T., Ogata, M., Aoki, Y., Imai, M., Fujimori, O., Katashiro, M., and Matsumoto, K. A MEMS Electromagnetic Optical Scanner for a Commercial Confocal Laser Scanning Microscope, *J. Microelectro. Sys.*, **12**, 243-251 (2003).

- [6] Yalcinkaya, A. D., Urey, H., Brown, D., Montague, T. and Sprague, R. Two-Axis Electromagnetic Microscanner for High Resolution Displays, *J. Microelectro. Sys.*, **15**, 786-794 (2006).
- [7] Chellappan, K. V., Erden, E. and Urey, H. Laser-based displays: a review, *Appl. Opt.*, **49**, F79-F98 (2010).
- [8] Meyer, R. A. Optical Beam Steering Using a Multichannel Lithium Tantalate Crystal, *Appl. Opt.*, **11**, 613-616 (1972).
- [9] Resler, D. P., Hobbs, D. S., Sharp, R. C., Friedman, L. J. and Dorschner, T. A. High-efficiency liquid-crystal optical phased-array beam steering, *Opt. Lett.*, **21**, 689-691 (1996).
- [10] Thomas, J. A. and Fainman, Y. Optimal cascade operation of optical phased-array beam deflectors, *Appl. Opt.*, **37**, 6196-6212 (1998).
- [11] Xiao, F., Hu, W. and Xu, A. Optical phased-array beam steering controlled by wavelength, *Appl. Opt.*, **44**, 5429-5433 (2005).
- [12] Acoleyen, K. V., Bogaerts, W., Jágerská, J., Thomas, N. L., Houdré, R. and Baets, R. Off-chip beam steering with a one-dimensional optical phased array on silicon-on-insulator, *Opt. Lett.*, **34**, 1477-1479 (2009).
- [13] Acoleyen, K. V., Rogier, H. and Baets, R. Two-dimensional optical phased array antenna on silicon-on-insulator, *Opt. Exp.*, **18**, 13655-13660 (2010).
- [14] Kwong, D., Hosseini, A., Zhang, Y. and Chenb, R. T. 1×12 Unequally spaced waveguide array for actively tuned optical phased array on a silicon nanomembrane, *Appl. Phys. Lett.*, **99**, 051104 (2011).
- [15] Doylend, J. K., Heck, M. J. R., Bovington, J. T., Peters, J. D., Coldren, L. A. and Bowers, J. E. Two-dimensional free-space beam steering with an optical phased array on silicon-on-insulator, *Opt. Exp.*, **19**, 21595-21604 (2011).
- [16] Sun, J., Timurdogan, E., Yaacobi1, A., Hosseini, E. S., and Watts, M. R. Large-scale nanophotonic phased array, *Nature*, **493**, 195-199 (2013).
- [17] Gu, X., Shimada, T. and Koyama, F. Giant and high-resolution beam steering using slow-light waveguide amplifier, *Opt. Exp.*, **19**, 22675-22683 (2011).
- [18] Gu, X., Shimada, T., Matsutani, A. and Koyama, F. Ultra-high channel-count wavelength demultiplexer based on a Bragg reflector waveguide with large angular dispersion, *Opt. Exp.*, **20**, B331-B338 (2012).
- [19] Ito, H., Kusunoki, Y., Maeda, J., Akiyama, D., Kodama, N., Abe, H., Tetsuya, R. and Baba, T. Wide beam steering by slow-light waveguide gratings and a prism lens, *Optica*, **7**, 47-52 (2020).
- [20] Scrymgeour, D. A., Barad, Y., Gopalan, V., Gahagan, K. T., Jia, Q., Mitchell, T. E. and Robinson, J. M. Large-angle electro-optic laser scanner on LiTaO₃ fabricated by *in situ*

- monitoring of ferroelectric-domain micropatterning, *Appl. Opt.*, **40**, 6236-6241 (2001).
- [21] Nakamura, K., Miyazu, J., Sasaura, M., and Fujiura, K. Wide-angle, low-voltage electro-optic beam deflection based on space-charge-controlled mode of electrical conduction in $\text{KTa}_{1-x}\text{Nb}_x\text{O}_3$, *Appl. Phys. Lett.*, **89**, 131115 (2006).
- [22] Kurosaka, Y., Iwahashi, S., Liang, Y., Sakai, K., Miyai, E., Kunishi, W., Ohnishi, D. and Noda, S. On-chip beam-steering photonic-crystal lasers, *Nature Photo.*, **4**, 447-450 (2010).
- [23] Nishiwaki, S., Asada, J. and Uchida, S. Optical Head Employing Concentric-Circular Focusing Grating Coupler, *Appl. Opt.*, **33**, 1819-1827 (1994).
- [24] Nishiwaki, S. Aberrations and convergence characteristics of a concentric-circular focusing grating coupler, *Appl. Opt.*, **34**, 7361-7371 (1995).
- [25] Nishiwaki, S., Asada, J., Ooshima, K. and Kitagawa, T. Fabrication of a concentric-circular focusing grating coupler utilizing a conic-wavefront interference method, and light convergence experiments using the coupler, *Appl. Opt.*, **34**, 7372-7382 (1995).

Figure legends

Figure 1. Structure and operational principles of CGC-LIDAR

a. Perspective illustration of a CGC-LIDAR

The circularly polarized light vertically incident to coupler A excites a guided light which propagates uniformly from the center to outside. The guided light is radiated from coupler C, concentrated near point F_1 , and converted to 2D-scannable five parallel beams by refraction at the side surfaces of the rod lens.

b. Cross-sectional illustration of a CGC-LIDAR

Concentric circular gratings are formed on the $\text{Ta}_2\text{O}_5 / \text{SiO}_2$ layers of the quartz plate and on the ITO / SiN layers of the HR plate. Gratings for the $\text{Ta}_2\text{O}_5 / \text{SiO}_2$ layers and electrodes are divided from the inside to outside into the three areas of A, B, and C. The LC layer sandwiched by the two plates is homogeneously aligned along the rotational direction around the axis L due to the orientation force of the gratings. CGC-LIDAR is built up concentrically with an RLE and a CGCP which are joined with a matching oil.

c. Perspective-view SEM photographs of coupler A

d. Top-view SEM photograph of coupler A

e. Configuration diagram of electrodes for areas A, B, and C

The electrode B is divided into 60 areas of B_k ($k = 0$ to 59) in the rotational direction.

While the electrodes A and C, shaped as circles or half rings, have the same shapes between the Al layer and the ITO layer, the B_k electrodes with a zigzag shape are reversed between them. The electrode C is divided in half and the gaps between them are used for the wires

of electrodes A and B_k . Since the AC signals applied to the electrodes are reversed between the Al electrode and the ITO electrode, the differences in voltages between them are doubled.

f. Relationships between effective refractive index (ERI) and waveguide thickness

When AC signals are applied to the electrodes, the LC alignment is raised, and ERI falls in inverse proportion to the AC amplitude.

Figure 2. Beam-condensing and rotating principle in the horizontal direction

a. Electrode pairs composed of upper and lower electrodes B_k and a trace of guided light

Electrodes b_{2k} are generated from the combination of Al electrodes B_k and ITO electrodes B_k , and electrodes b_{2k+1} are from Al electrodes B_k and ITO electrodes B_{k+1} . In response to the voltages v_{2k} or v_{2k+1} at electrodes b_{2k} or b_{2k+1} , the ERIs of N_{2k} or N_{2k+1} are aligned in the radial direction. The guided light deflects to the higher-index side at the intersection with the boundary of the diamond-shaped electrodes, as shown by the red arrow.

b. Examples of voltage waveforms applied to the B_k electrodes

Amplitude distribution between the electrodes B_k allows the beams to be collimated. Collimated beams can be rotated by applying a phase-shift signal to the neighbor electrodes.

c. Relationships under a static condition between a voltage waveform and the response of the ERI to an azimuth angle φ

The waveform is represented by a collection of voltage elements v_{2k} and v_{2k+1} which are applied to the electrodes b_{2k} and b_{2k+1} . The curve of ERI traces a shape that is the inverse of waveform V_B .

d. Perspective illustration of light radiated from the coupler C and a cross-sectional drawing of light refracted at the rod lens surface

When applied to the B_k electrodes, the radiated light is focused on point F_1 and becomes a parallel beam after refraction at the side surface of the rod lens.

e. Ray-traced result for light that propagates in the guided layer and penetrates the RLE

This is an example for $m = 5$. In the range of $\varphi = -36$ to 36 degrees, the guide light is convergent and radiates from the coupler C. It becomes a parallel beam after focusing at point F_1 and passing through the rod lens. This situation is similar in the other angular ranges and five parallel beams are produced in total.

f. Necessary shape of the curve of the ERI difference

Figure 3. Analytical results for input- and output-coupling characteristics

a. Response of input-coupling efficiency at coupler A to a buffer layer thickness t_0

This is calculated by 3D-FDTD for $\lambda = 0.94 \mu\text{m}$, $\Lambda = 0.54$ and $0.55 \mu\text{m}$, $t_1 = 0.14 \mu\text{m}$,

groove depth $d = 0.1 \mu\text{m}$, groove duty rate $\varepsilon = 0.5$, and diameter $L = 10 \mu\text{m}$: $t_0 = 1.16 \mu\text{m}$ is appropriate for counteracting film thickness error.

b. Responses of input-coupling efficiency at coupler A to coupling length L

This is calculated by 2D-FDTD for $\lambda = 0.94 \mu\text{m}$, $\Lambda = 0.55 \mu\text{m}$, $t_1 = 0.14 \mu\text{m}$, $t_0 = 1.16 \mu\text{m}$, $d = 0.02 \mu\text{m}$, and $\varepsilon = 0.5$.

c. Responses of input-coupling efficiency at coupler A to wavelength λ

This is calculated by 2D-FDTD for $\Lambda = 0.54$ and $0.55 \mu\text{m}$, $d = 0.02 \mu\text{m}$, $\varepsilon = 0.5$, $t_1 = 0.14 \mu\text{m}$, $t_0 = 1.16 \mu\text{m}$, and coupling length $L = 90 \mu\text{m}$. $L = 90 \mu\text{m}$ and $\Lambda = 0.544 \mu\text{m}$ are appropriate for maximizing the coupling efficiency.

d, e, and f. Responses of radiation decay factor α to groove depth d (where $\varepsilon = 0.5$ and $n_L = 1.60$), groove duty rate ε (where $d = 0.02 \mu\text{m}$ and $n_L = 1.60$), and LC index n_L (where $d = 0.02 \mu\text{m}$ and $\varepsilon = 0.25$)

These are calculated by 2D-FDTD for $\Lambda = 0.30 \mu\text{m}$, $t_1 = 0.14 \mu\text{m}$, and $t_0 = 1.16 \mu\text{m}$: factor α for coupler C can be brought below 2mm^{-1} by adopting the design condition of $d = 0.02 \mu\text{m}$ and $\varepsilon = 0.2$.

Figure 4. Experimental system for observation of scanning beams

a. Configuration diagram of the experimental system

Light radiated from coupler C is converted from rotation at a constant angular velocity to a linear uniform motion by an f - θ lens and is observed using an imaging camera.

b, c, and d. Perspective photographs of a portion of the experimental system, the RLE, and the CGCP

e. Photograph for a central surface of the CGCP under LC control, with RLE removed

f. Observation photograph of a light spot incident to the surface of the CGCP using a microscope

Figure 5. Observation results

a. Relationship between the amount of light radiated from the coupler C and the constant voltage applied to the electrodes B_k with the cycle t_B of triangular AC voltage as the parameter

b. Observation photograph indicating oriented states of the LC at the fringe region of the electrodes B and C

c and d. Displacement and spread angles of vertical steering beams for the voltage applied to the electrode C with the cycle t_C of rectangular AC voltage as a parameter

e1-e3 Observation photographs of vertically sweeping beams radiated from coupler C using the imaging camera of the f - θ lens. The beams sweep by a vibrating control of $T_C = 1.0 \text{ sec}$ and $V_C = 0 - 20.0 \text{ volts}$ for electrode C and the sweeping spots are generated by the light

propagating the area just visible in Fig. 5b.

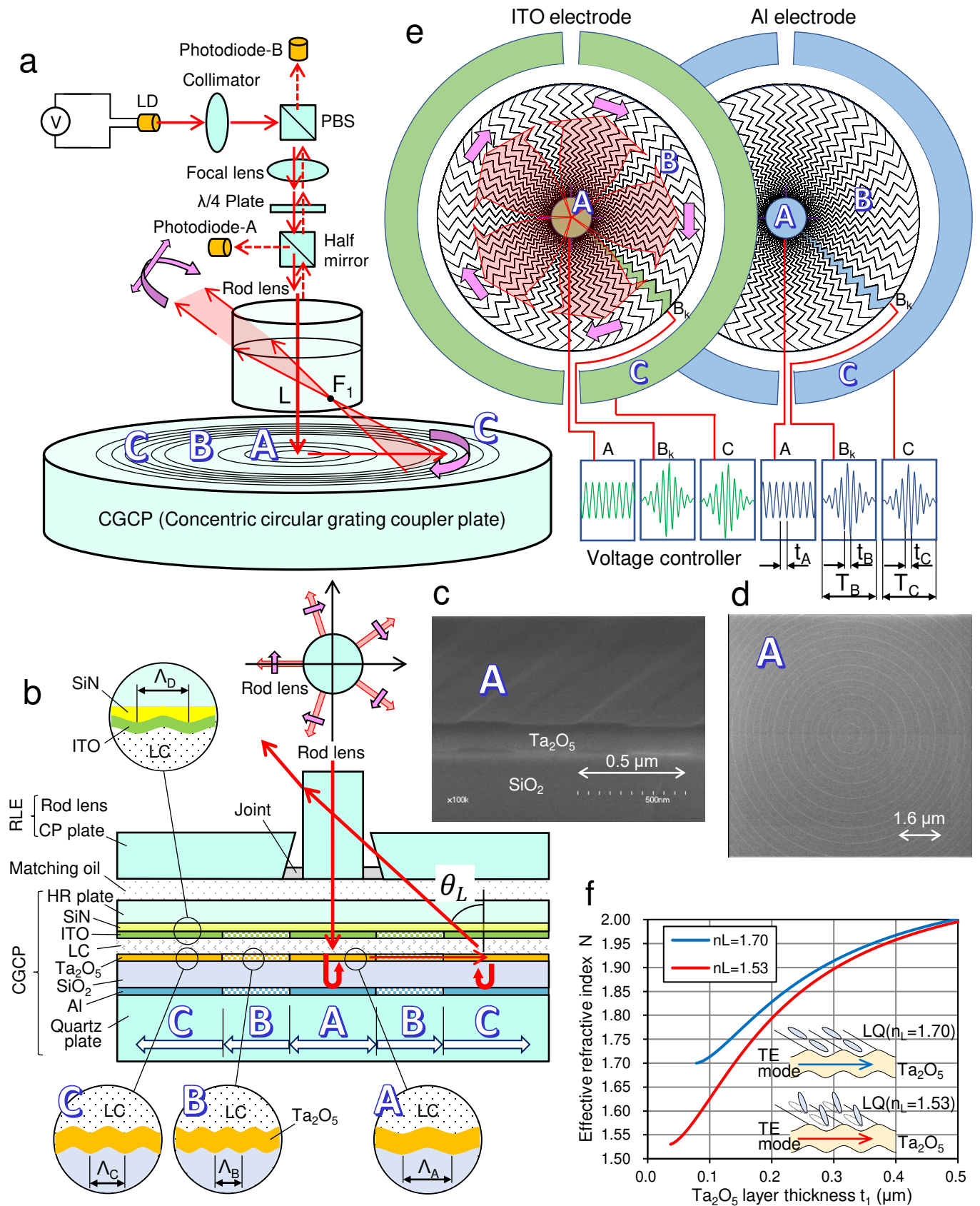
f. Frequency response of the vertical displacement. Half maximum of the displacement amplitude is maintained up to 100 Hz.

g. Observation photographs of rotationally sweeping beams radiated from coupler C using the imaging camera of the f- θ lens. The beams show rotational sweeps by the rotational state of $T_B = 0.5$ sec for electrode B and the static state of $t_C = 1/16$ ms and $V_C = 15.0$ volts for electrode C.

h. Image-analyzed results of a movie, showing amount of light. The beams sweep rotationally 10 times per turn.

i. Relationships between the spread angle and the rotating angle

Beams scan rotationally with a 6-degree cycle variation of spread angle of between 0.8 - 3.5 degrees.



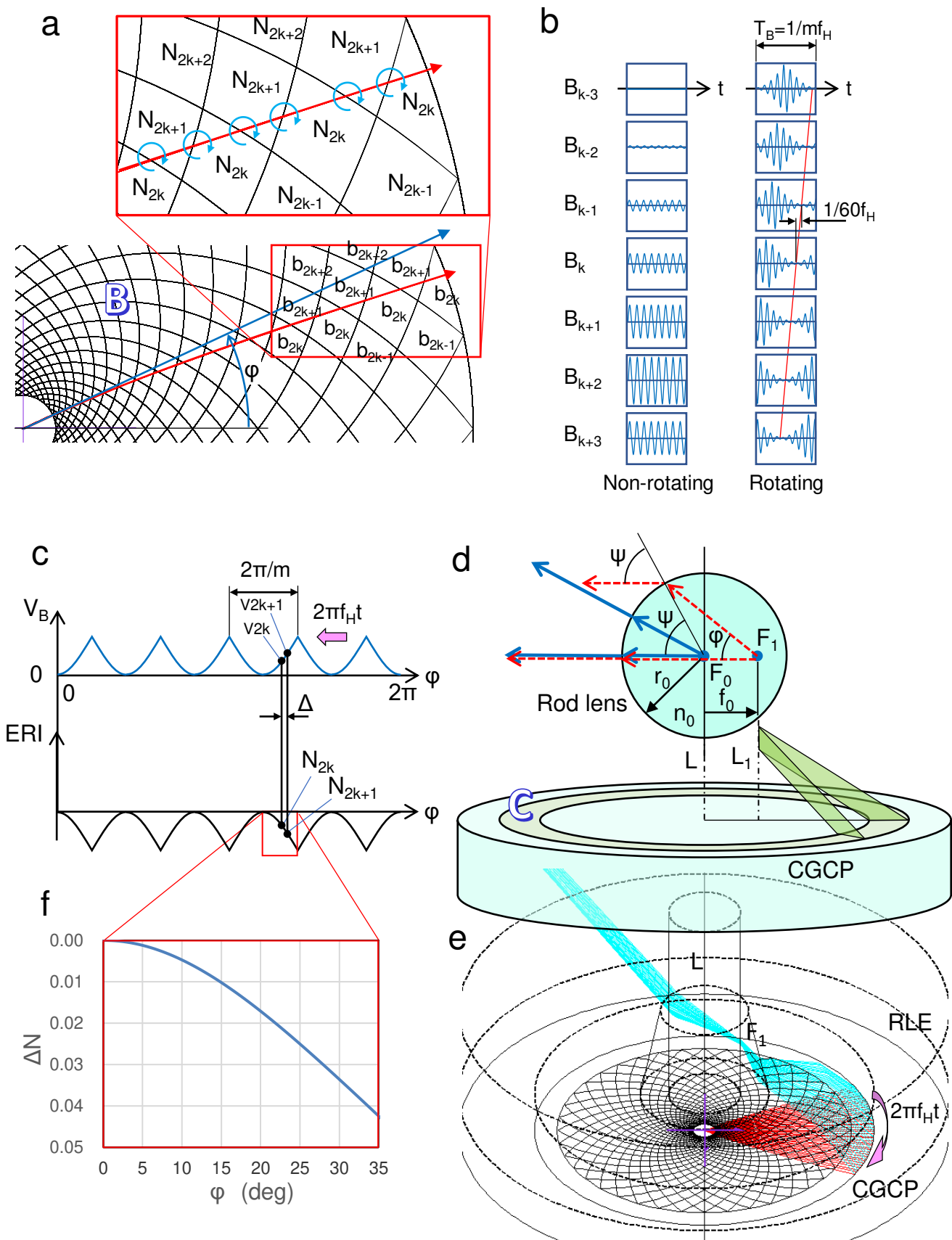


Figure 2. Beam-condensing and rotating principle in the horizontal direction

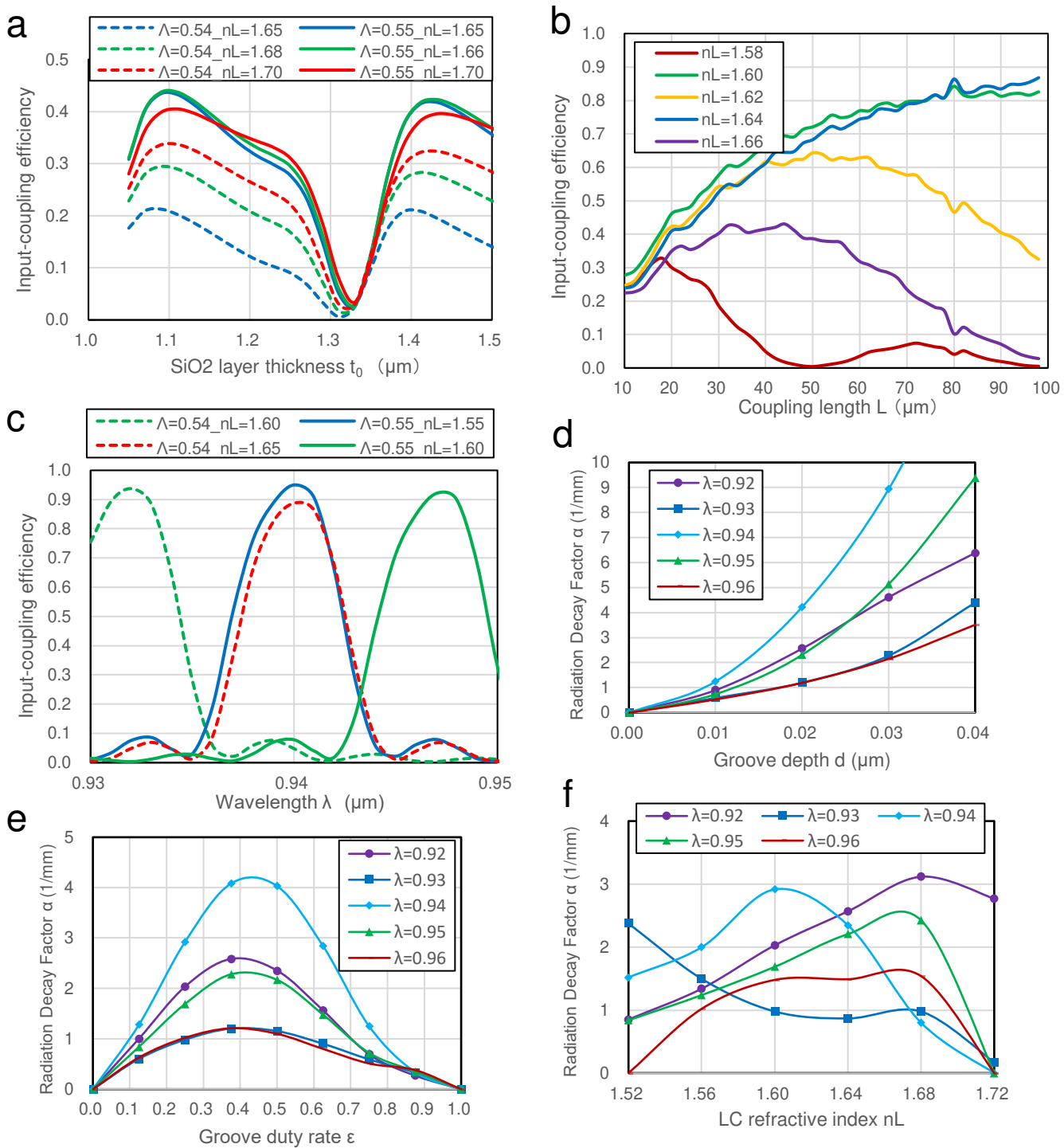


Figure 3. Analytical results for Input- and output-coupling characteristics

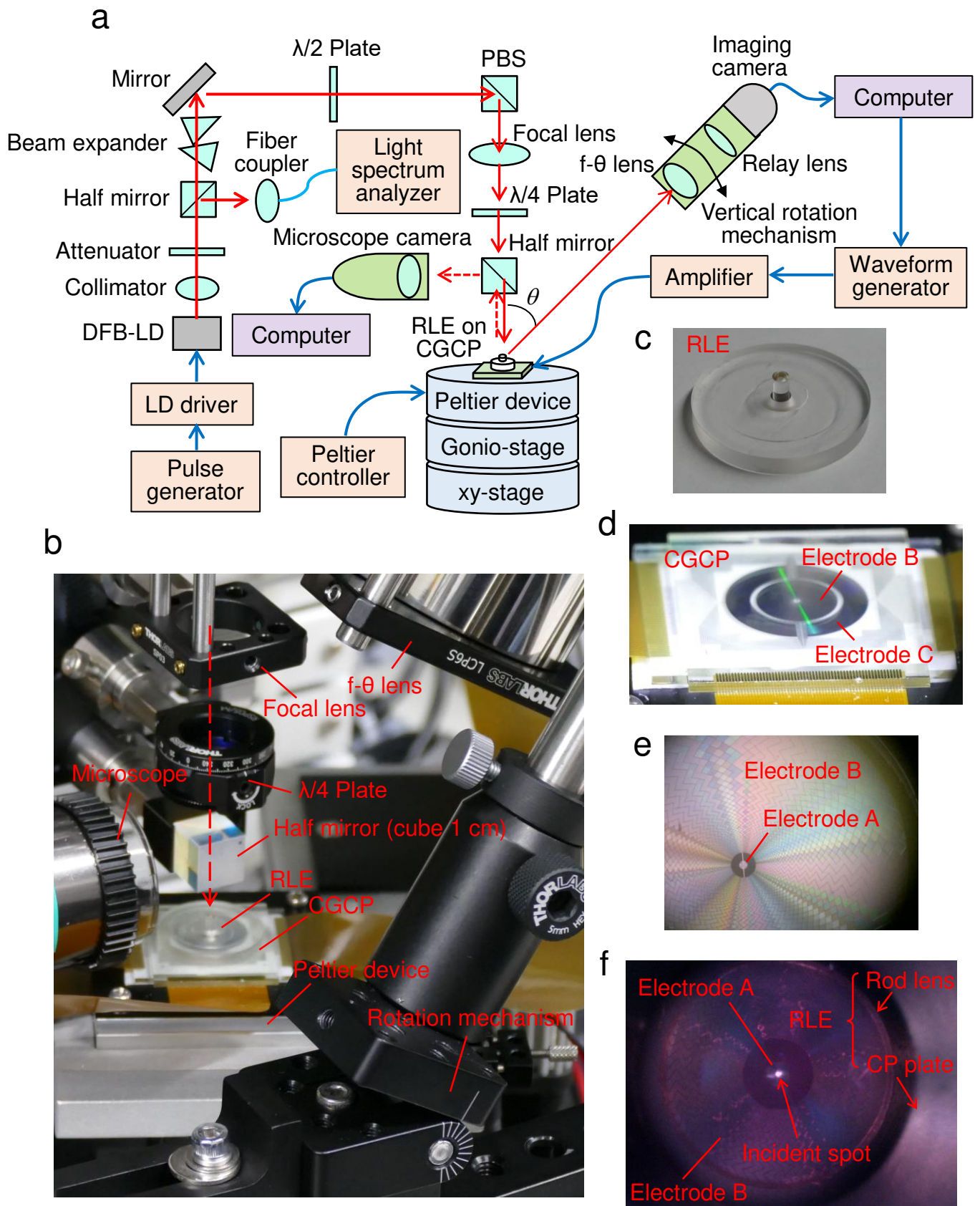


Figure 4. Experimental system for observation of scanning beams

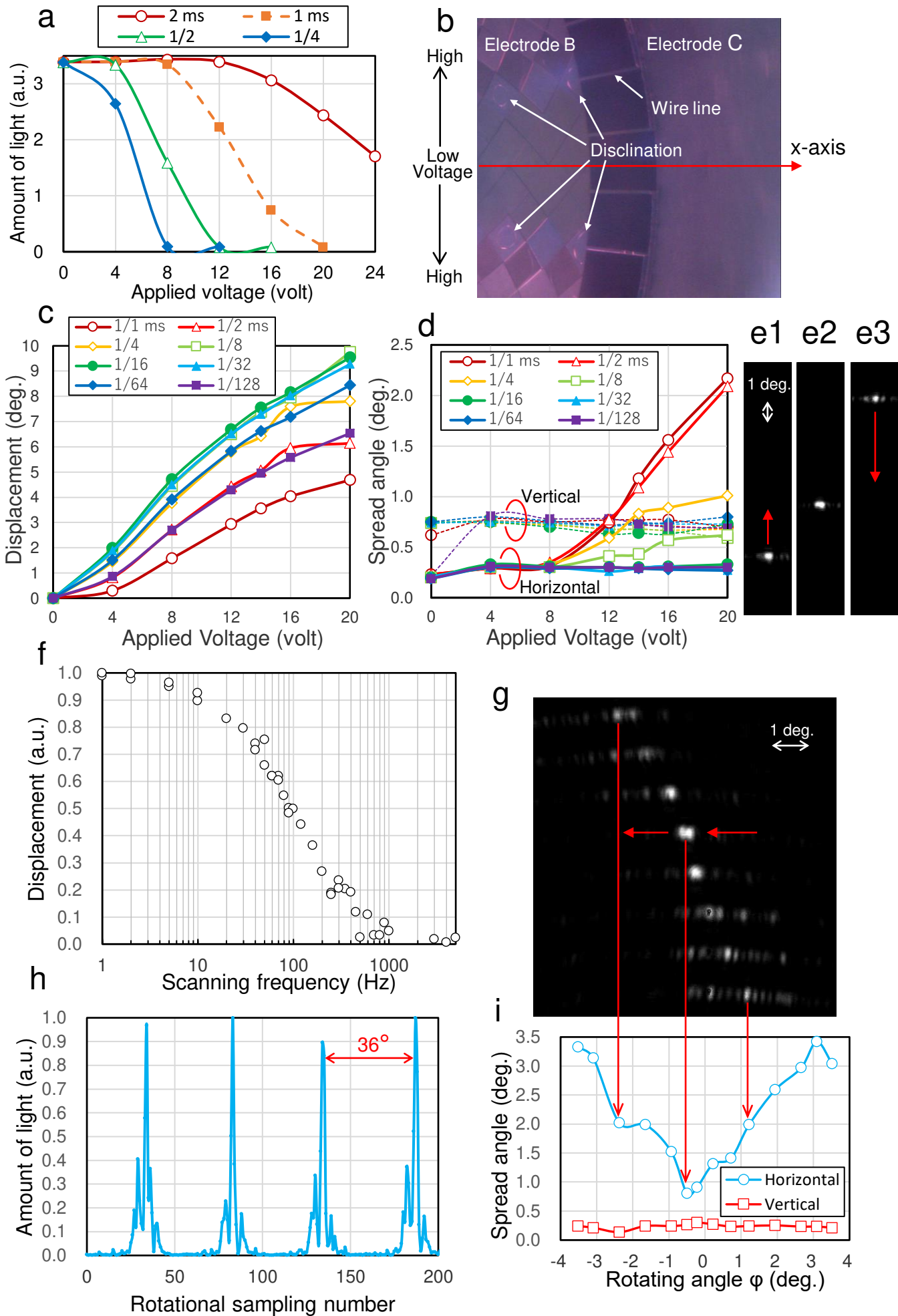


Figure 5. Observation results

Figures

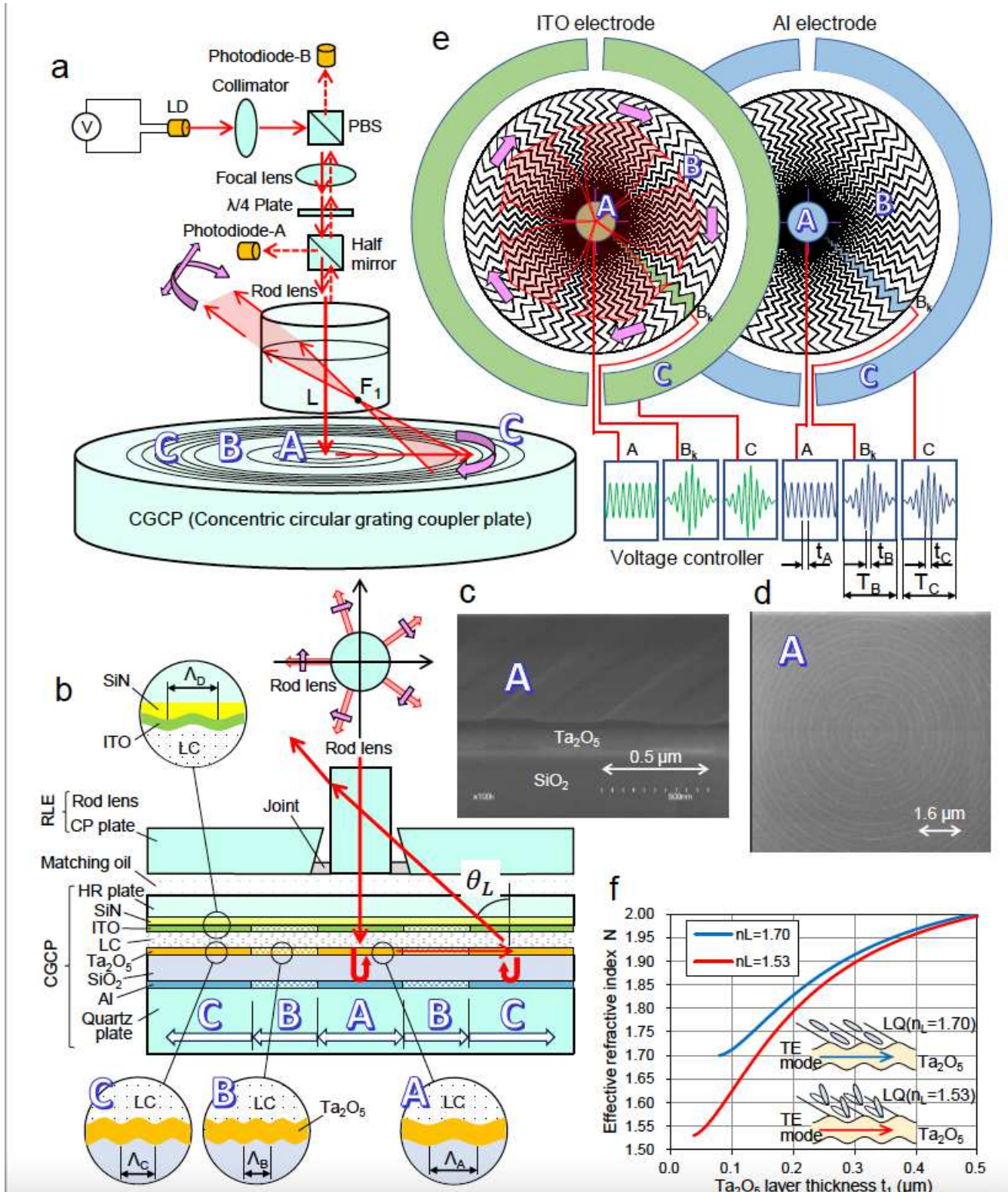


Figure 1

Structure and operational principles of CGC LIDAR a. Perspective illustration of a CGC LIDAR The circularly polarized light vertically incident to coupler A excites a guided light which propagates uniformly from the center to outside. The guided light is radiated from coupler C, concentrated near point F1, and

converted to 2D scannable five parallel beams by refraction at the side surfaces of the rod lens. b. Cross sectional illustration of a CGC LIDAR Concentric circular gratings are formed on the Ta₂O₅ / SiO₂ layers of the quartz plate and on the ITO / SiN layers of the HR plate. Gratings for the Ta₂O₅ / SiO₂ layers and electrodes are divided from the inside to outside into the three areas of A, B, and C. The LC layer sandwiched by the two plates is homogeneously aligned along the rotational direction around the axis L due to the orientation force of the gratings. CGC LIDAR is built up concentrically with an RLE and a CGCP which are joined with a matching oil. c. Perspective view SEM photographs of coupler A d. Top view SEM photograph of coupler A e. Configuration diagram of electrodes for areas A, B, and C The electrode B is divided into 60 areas of B_k (k = 0 to 59) in the rotational direction. While the electrodes A and C, shaped as circles or half rings, have the same shapes between the Al layer and the ITO layer, the B_k electrodes with a zigzag shape are reversed between them. The electrode C is divided in half and the gaps between them are used for the wires of electrodes A and B_k. Since the AC signals applied to the electrodes are reversed between the Al electrode and the ITO electrode, the differences in voltages between them are doubled. f. Relationships between effective refractive index (ERI) and waveguide thickness When AC signals are applied to the electrodes, the LC alignment is raised, and ERI falls in inverse proportion to the AC amplitude.

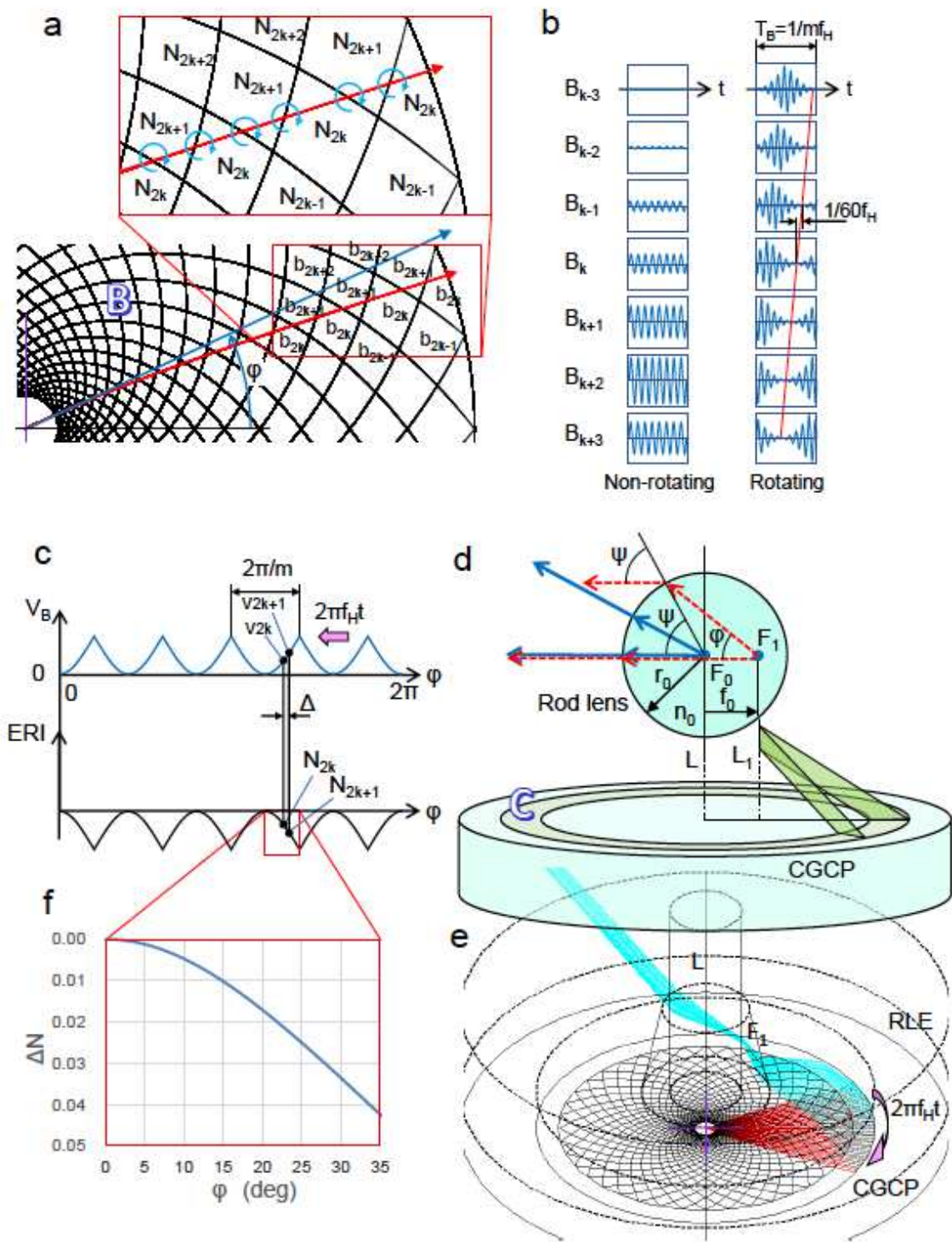


Figure 2

Beam condensing and rotating principle in the horizontal direction a. Electrode pairs composed of upper and lower electrodes B_k and a trace of guided light Electrodes b_{2k} are generated from the combination of Al electrodes B_k and ITO electrodes B_k , and electrodes b_{2k+1} are from Al electrodes B_k and ITO electrodes B_{k+1} . In response to the voltages v_{2k} or v_{2k+1} at electrodes b_{2k} or b_{2k+1} , the ERIs of N_{2k} or N_{2k+1} are aligned in the radial direction. The guided light deflects to the higher index side at the

intersection with the boundary of the diamond shaped electrodes, as shown by the red arrow. b. Examples of voltage waveforms applied to the Bk electrodes Amplitude distribution between the electrodes Bk allows the beams to be collimated. Collimated beams can be rotated by applying a phase shift signal to the neighbor electrodes. c. Relationships under a static condition between a voltage waveform and the response of the ERI to an azimuth angle φ The waveform is represented by a collection of voltage elements v_{2k} and v_{2k+1} which are applied to the electrodes b_{2k} and b_{2k+1} . The curve of ERI traces a shape that is the inverse of waveform VB. d. Perspective illustration of light radiated from the coupler C and a cross sectional drawing of light refracted at the rod lens surface When applied to the Bk electrodes, the radiated light is focused on point F1 and becomes a parallel beam after refraction at the side surface of the rod lens. e. Ray traced result for light that propagates in the guided layer and penetrates the RLE This is an example for $m = 5$. In the range of $\varphi = 36$ to 36 degrees, the guide light is convergent and radiates from the coupler C. It becomes a parallel beam after focusing at point F1 and passing through the rod lens. This situation is similar in the other angular ranges and five parallel beams are produced in total. f. Necessary shape of the curve of the ERI difference

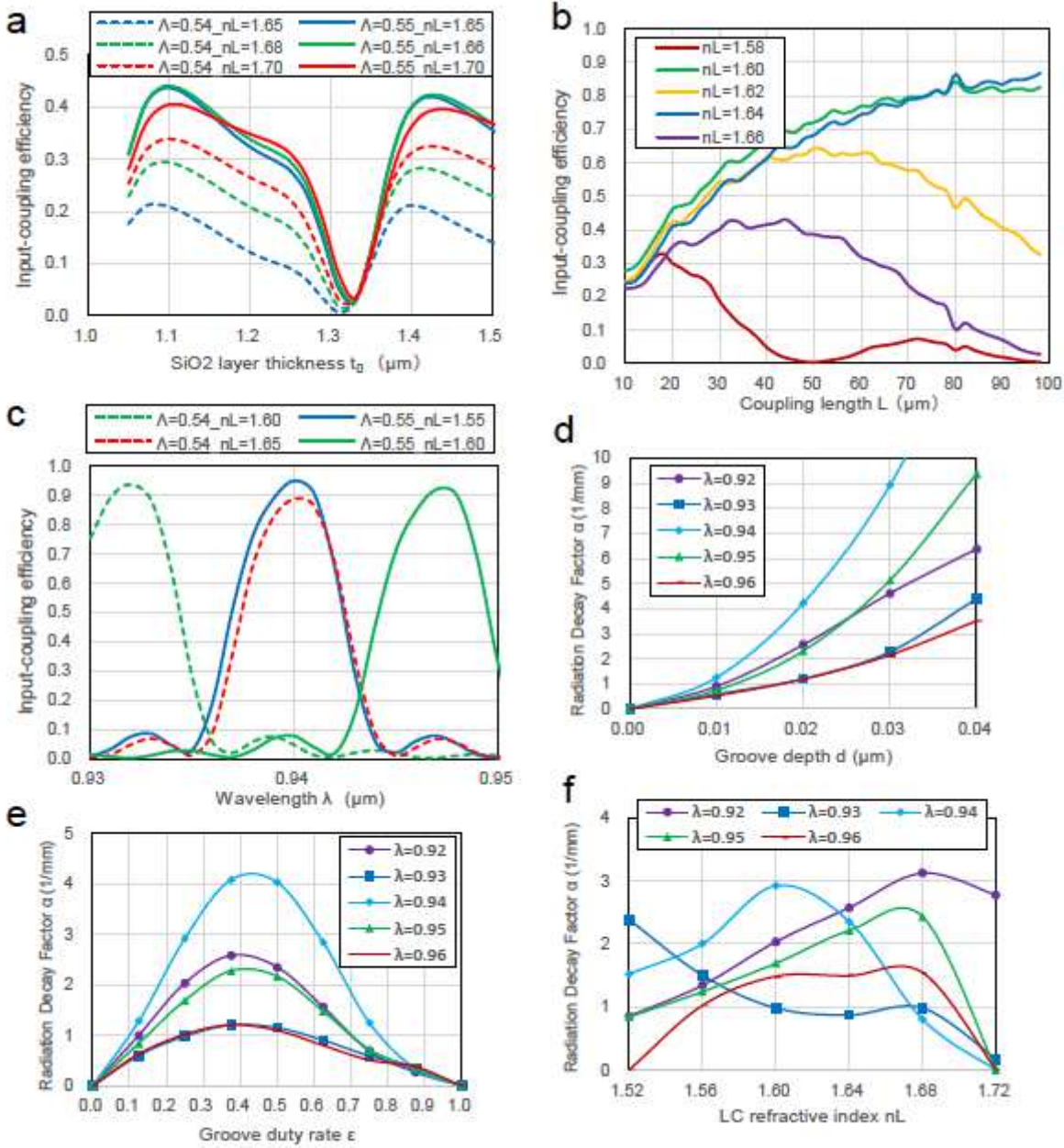


Figure 3

Analytical results for input and output coupling characteristics a. Response of input coupling efficiency at coupler A to a buffer layer thickness t_0 This is calculated by 3D FDTD for $\lambda = 0.94$ μm , $\Lambda = 0.54$ and 0.55 μm , $t_1 = 0.14$ μm , groove depth $d = 0.1$ μm , groove duty rate $\epsilon = 0.5$, and diameter $L = 10$ μm : $t_0 = 1.16$ μm is appropriate for counteracting film thickness error. b. Responses of input coupling efficiency at coupler A to coupling length L This is calculated by 2D FDTD for $\lambda = 0.94$ μm , $\Lambda = 0.55$ μm , $t_1 = 0.14$ μm , $t_0 = 1.16$ μm , $d = 0.02$ μm , and $\epsilon = 0.5$. c. Responses of input coupling efficiency at coupler A to wavelength λ This is calculated by 2D FDTD for $\Lambda = 0.54$ and 0.55 μm , $d = 0.02$ μm , $\epsilon = 0.5$, $t_1 = 0.14$ μm , $t_0 = 1.16$ μm , and coupling length $L = 90$ μm . $L = 90$ μm and $\Lambda = 0.544$ μm are appropriate for maximizing the coupling

efficiency. d , e , and f . Responses of radiation decay factor α to groove depth d (where $\epsilon = 0.5$ and $nL = 1.60$), groove duty rate ϵ (where $d = 0.02 \mu\text{m}$ and $nL = 1.60$), and LC index nL (where $d = 0.02 \mu\text{m}$ and $\epsilon = 0.25$) These are calculated by 2D FDTD for $\lambda = 0.30 \mu\text{m}$, $t_1 = 0.14 \mu\text{m}$, and $t_0 = 1.16 \mu\text{m}$: factor α for coupler C can be brought below 2 mm⁻¹ by adopting the design condition of $d = 0.02 \mu\text{m}$ and $\epsilon = 0.2$.

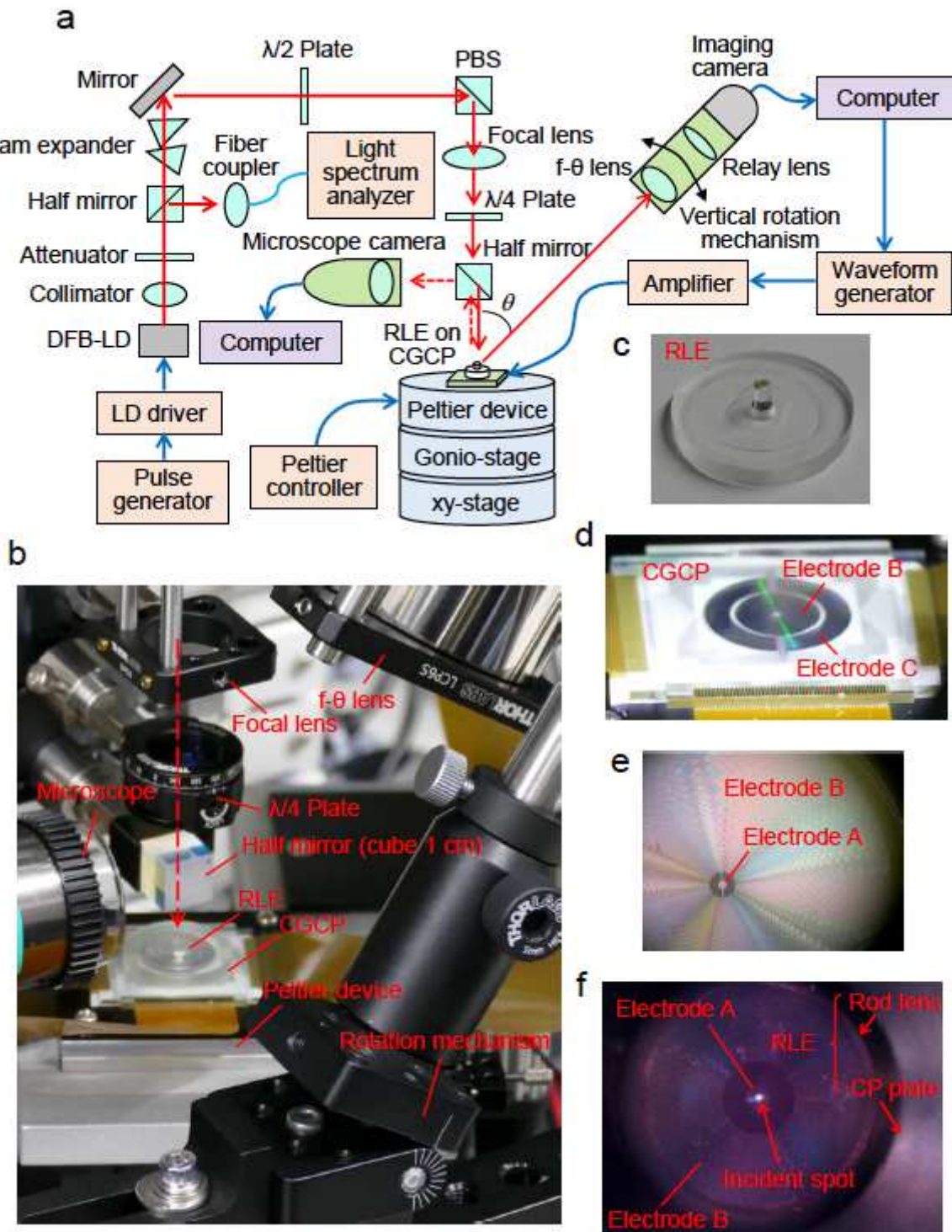


Figure 4

Experimental system for observation of scanning beams a. Configuration diagram of the experimental system Light radiated from coupler C is converted from rotation at a constant angular velocity to a linear uniform motion by an $f \theta$ lens and is observed using an imaging camera. b, c, and d. Perspective photographs of a portion of the experimental system, the RLE, and the CGCP e. Photograph for a central surface of the CGCP under LC control, with RLE removed f. Observation photograph of a light spot incident to the surface of the CGCP using a microscope

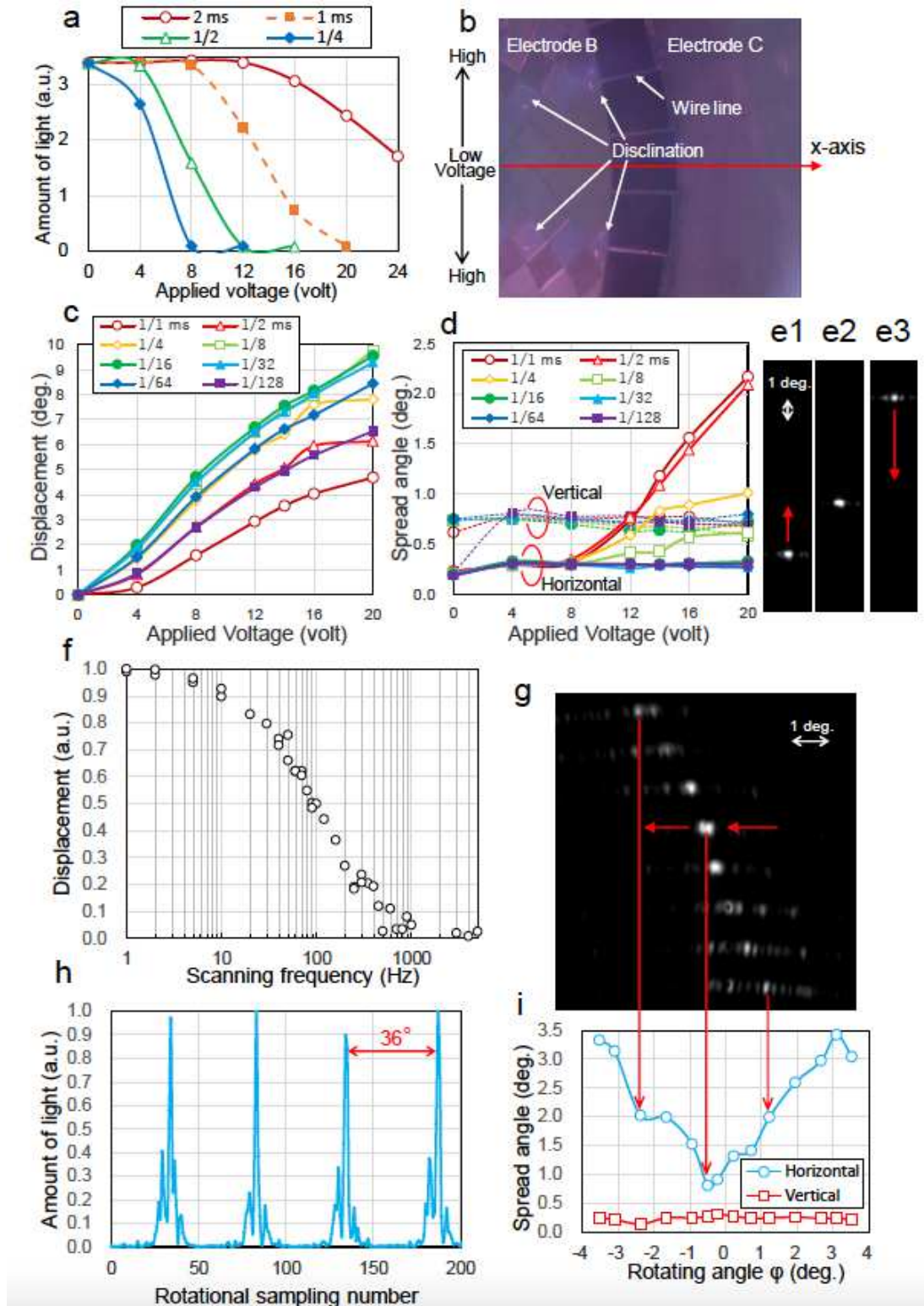


Figure 5

Observation results a. Relationship between the amount of light radiated from the coupler C and the constant voltage applied to the electrodes Bk with the cycle tB of triangular AC voltage as the parameter b. Observation photograph indicating oriented states of the LC at the fringe region of the electrodes B and C c and d. Displacement and spread angles of vertical steering beams for the voltage applied to the electrode C with the cycle tC of rectangular AC voltage as a parameter e1 e3 Observation photographs of vertically sweeping beams radiated from coupler C using the imaging camera of the f θ lens. The beams sweep by a vibrating control of TC = 1.0 sec and VC = 0 20.0 volts for electrode C and the sweeping spots are generated by the light propagating the area just visible in Fig. 5b. f. Frequency response of the vertical displacement. Half maximum of the displacement amplitude is maintained up to 100 Hz. g. Observation photographs of rotationally sweeping beams radiated from coupler C using the imaging camera of the f θ lens. The beams show rotational sweeps by the rotational state of TB = 0.5 sec for electrode B and the static state of tC = 1/16 ms and VC = 15.0 volts for electrode C. h. Image analyzed results of a movie, showing amount of light. The beams sweep rotationally 10 times per turn. i. Relationships between the spread angle and the rotating angle Beams scan rotationally with a 6 degree cycle variation of spread angle of between 0.8 - 3.5 degrees.

Supplementary Files

This is a list of supplementary files associated with this preprint. Click to download.

- [Supplementaryall.pdf](#)
- [M1.mp4](#)
- [M2.mp4](#)
- [M3.mp4](#)